Monthly Notices
of the
ROYAL ASTRONOMICAL SOCIETY

Mon. Not. R. Astron. Soc. **422,** 367–378 (2012) doi:10.1111/j.1365-2966.2012.20615.x

First Very Large Telescope/X-shooter spectroscopy of early-type stars outside the Local Group⋆

O. E. Hartoog,[1]† H. Sana,[1] A. de Koter[1,2] and L. Kaper[1]

[1]*Astronomical Institute 'Anton Pannekoek', University of Amsterdam, Science Park 904, 1098 XH Amsterdam, the Netherlands*
[2]*Astronomical Institute, Utrecht University, Princetonplein 5, 3584 CC Utrecht, the Netherlands*

Accepted 2012 January 21. Received 2012 January 20; in original form 2011 November 2

ABSTRACT

As part of the Very Large Telescope (VLT)/X-shooter science verification, we obtained the first optical medium-resolution spectrum of a previously identified bright O-type object in NGC 55, a Large Magellanic Cloud (LMC)-like galaxy at a distance of ∼2.0 Mpc. Based on the stellar and nebular spectra, we investigate the nature and evolutionary status of the central object(s) and its influence on the surrounding interstellar medium. We conclude that the source, NGC 55 C1_31, is a composite object, likely a stellar cluster, which contains one or several hot ($T_{\rm eff} \simeq 50\,000$ K) WN stars with a high mass-loss rate ($\sim 3 \times 10^{-5}\,{\rm M}_\odot\,{\rm yr}^{-1}$) and a helium-rich composition ($N_{\rm He}/N_{\rm H} = 0.8$). The visual flux is dominated by OB-type (super)giant stars with $T_{\rm eff} \lesssim 35\,000$ K, solar helium abundance ($N_{\rm He}/N_{\rm H} = 0.1$) and mass-loss rate $\sim 2 \times 10^{-6}\,{\rm M}_\odot\,{\rm yr}^{-1}$. The surrounding H II region has an electron density of $n_{\rm e} \leq 10^2\,{\rm cm}^{-3}$ and an electron temperature of $T({\rm O\,III}) \simeq 11\,500 \pm 600$ K. The oxygen abundance of this region is [O/H] $= 8.18 \pm 0.03$, which corresponds to $Z = 0.31 \pm 0.04\,{\rm Z}_\odot$. We observed no significant gradients in $T({\rm O\,III})$, $n_{\rm e}$ or [O/H] on a scale of 73 pc extending in four directions from the ionizing source. The properties of the H II region can be reproduced by a CLOUDY model which uses the central cluster as ionizing source, thus providing a self-consistent interpretation of the data. We also report on the serendipitous discovery of He II nebular emission associated with the nearby source NGC 55 C2_35, a feature usually associated with strong X-ray sources.

Key words: stars: early type – stars: individual: NGC 55 C1_31 – stars: massive – stars: Wolf–Rayet – H II regions – galaxies: individual: NGC 55.

1 INTRODUCTION

The most luminous stars in low-metallicity galaxies are of special interest. These may have masses exceeding 200 $\rm M_\odot$, defining the upper mass limit of stars. Until recently, such massive objects were only found in the cores of young massive clusters (Crowther et al. 2010), but the first such object has now been found in apparent isolation (Bestenlehner et al. 2011). This motivates a search for very massive stars in Local Group dwarf galaxies, or even more distant systems, where current instrumentation does not yet allow stellar clusters to be spatially resolved. Depending on mass and metallicity, the mass-loss rates of the brightest stars may be so high that their winds become optically thick, resulting in hydrogen-rich WN spectra (de Koter, Heap & Hubeny 1997). Such targets provide important tests for the theory of line-driven winds (Gräfener et al. 2011; Vink et al. 2011). Massive stars up to about 80 $\rm M_\odot$ in metal-poor environments receive special attention as well, as those that have a rapidly rotating core at the end of their lives may produce broad-line Type Ic supernovae or hypernovae, which are perhaps connected to long-duration gamma-ray bursts (Moriya et al. 2010).

In this context, massive stars in the Magellanic Clouds have been extensively studied (see e.g. Evans et al. 2004, 2011). Extending such studies to more distant galaxies requires sensitive spectrographs mounted at the largest telescopes and, so far, has only been attempted at low resolution (Bresolin et al. 2006, 2007; Castro et al. 2008). Such low-resolution studies can be hampered by the presence of nebular emission, as due to their strong ultraviolet (UV) flux, massive stars ionize the ambient environment creating H II regions. Through observations at higher spectral resolution, nebular emission, rather than being a complicating factor, may help to further constrain physical properties of the ionizing source (see e.g. Kudritzki & Hummer 1990).

In this paper, we take the first step towards quantitative spectroscopy of massive stars outside the Local Group. We present the first medium-resolution spectrum of a luminous early-type source in

⋆Based on observations made with ESO Telescopes at the Paranal Observatory under programme 60.A-9419(A).
†E-mail: O.E.Hartoog@uva.nl

NGC 55 (∼2.0 Mpc) and its surrounding region, obtained with the new X-shooter spectrograph at the European Southern Observatory (ESO) Very Large Telescope (VLT). The medium spectral resolution ($R \sim 6000$) and unique spectral coverage of X-shooter allow for a detailed analysis of the stellar spectrum, and, importantly, for an improved correction of the nebular emission lines that can be distinguished from the underlying stellar spectrum.

1.1 NGC 55

NGC 55 (see Fig. 1) is located in the foreground of the Sculptor Group, at a distance of approximately 2.0 Mpc (Gieren et al. 2008, and references therein). Though it is difficult to determine its morphological type due to its high inclination of ∼80° (Hummel, Dettmar & Wielebinski 1986), the galaxy is likely of type SB(s)m: a barred spiral with an irregular appearance, very similar to the Large Magellanic Cloud (de Vaucouleurs & Freeman 1972). Metallicity measurements of NGC 55 show a range of values between 0.23 and 0.7 $Z_{\odot}$, all determined by an analysis of forbidden oxygen line emission (see e.g. Webster & Smith 1983; Stasińska, Comte & Vigroux 1986; Zaritsky, Kennicutt & Huchra 1994; Tüllmann et al. 2003).

The blue massive star population of NGC 55 has been studied in the context of the Araucaria project (Gieren et al. 2005). As part of this project, Castro et al. (2008) have presented low-resolution ($R = 780$) UV–optical (390–490 nm) spectra of approximately 200 blue massive stars in NGC 55, taken with the Focal Reducer and low dispersion Spectrograph 2 (FORS2) on the VLT. In search for the most massive star in this galaxy, we selected NGC 55 C1_31 (for the remainder of this paper C1_31; RA 0:15:00.01, Dec. −39:12:41.39, indicated in Fig. 1) because of its brightness and its classification as an early O-type supergiant.

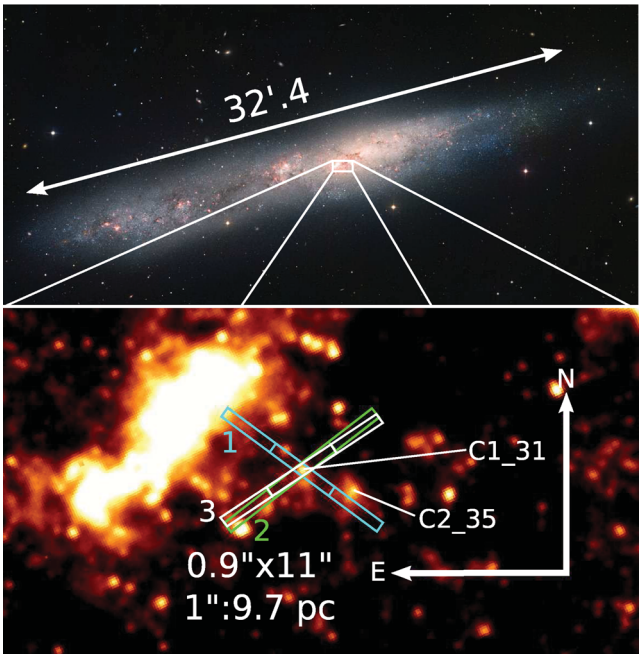

Figure 1. $B - V - H\alpha$ image of the host galaxy NGC 55 (MPG/ESO, Wide Field Imager) with a zoomed-in region (FORS Hα image) that indicates the location of our source. The rectangles show the projections of the VIS entrance slit (0.9×11 arcsec^2) at the different observing epochs: 1, 2009 August 13; 2, 2009 September 27; and 3, 2009 September 30. C1_31 is located where the slit projections cross. C2_35 is another massive star candidate, of which we see the surrounding nebular emission in our slit (see Section 4.2).

In the following section, we describe the observations and data reduction for both the stellar spectrum (Section 2.1) and the nebular spectra as a function of location along the slit (Section 2.2). In Section 3, we constrain the overall properties of the central source by comparing the observed hydrogen and helium line profiles of C1_31 with simulated profiles. In Section 4, we analyse the nebular spectra. In Section 5, we explore the effect of luminosity and temperature of the ionizing source on the properties of the surrounding nebula, resulting in a consistent picture on both the properties of the central ionizing source and the surrounding nebula (Section 6). We summarize the main results in Section 7.

2 OBSERVATIONS AND DATA REDUCTION

The observations of C1_31 were obtained as part of X-shooter Science Verification (SV) runs 1 and 2. Spread over three nights, the total exposure time is 2.5 h. The observations were carried out in nodding mode using a nod throw of 5 arcsec. We refer to Table 1 for the details of the observations and the observing conditions.

Light that enters X-shooter is split in three arms using dichroics: Ultra Violet-blue (UVB), VISual (VIS) and Near-infrared (NIR). Each instrument arm is a fixed-format cross-dispersed échelle spectrograph (D'Odorico et al. 2006; Vernet et al. 2011). Table 2 gives for each arm the wavelength range, the projected dimensions of the slit and the resolving power. The data are reduced with X-shooter pipeline version 1.2.2 (Modigliani et al. 2010; Goldoni 2011). Although our source is observed in nodding mode, we have reduced the UVB and VIS science frames separately, using the staring mode reduction recipe. We follow the full cascade of X-shooter pipeline steps ('physical model mode'), up to obtaining two-dimensional (2D) straightened spectra, without sky subtraction. See Section 2.1 for the steps through which we obtain the stellar spectrum of C1_31,

Table 1. Overview of the observations. Column 1: date and mid-exposure time of the observations; column 2: seeing measured from 2D spectrum spatial profiles; column 3: angular distance from the source to the Moon and fraction of lunar illumination (FLI); column 4: exposure time per arm; column 5: position angle (north to east) of the slit on the sky (along the parallactic angle at the time of the observations).

	Date Time (UT)	Seeing (R band)	Moon dist. FLI	Exposure time (s)	PA
1	13/08/09 08:52	0.69 − 0.88 arcsec	69° 56 per cent	2 × 900	53.°4
2	27/09/09 03:43	0.87 − 0.93 arcsec	66° 60 per cent	4 × 900	−52.°3
3	30/09/09 03:26	0.96 − 1.50 arcsec	45° 85 per cent	4 × 900	−56.°4

Table 2. Overview of X-shooter instrument properties. Column 1: instrument arm; column 2: wavelength range; column 3: projected slit size; column 4: measured resolving power $R = \lambda/\Delta\lambda$; column 5: resolving power according to X-Shooter User Manual.

Arm	Range (nm)	Slit dimensions (arcsec^2)	R	$R_{\rm th}$
UVB	300 − 560	0.8 × 11	6268 ± 179	6200
VIS	550 − 1020	0.9 × 11	7778 ± 264	8800
NIR	1020 − 2480	0.6 × 11	7650 ± 258	8100

Table 3. S/N per resolution element of different parts of the UVB and VIS spectra per night, and of the final combined spectra.

UVB arm			
	S/N [range (nm)]		
Night	[424:428]	[460:465]	[505:510]
13/08/09	16.9	21.3	21.4
27/09/09	14.0	21.2	13.7
30/09/09	7.2	9.8	9.8
Combined	21.2	29.3	27.4

VIS arm				
	S/N [range (nm)]			
Night	[604:609]	[675:680]	[811:816]	[975:978]
13/08/09	12.1	15.5	22.0	6.3
27/09/09	10.3	12.0	19.8	5.2
30/09/09	6.2	9.8	13.3	4.8
Combined	16.2	20.9	30.0	8.7

and Section 2.2 for the extraction procedure of the nebular spectra along the spatial direction of the slit.

2.1 The sky-corrected stellar spectrum

2.1.1 UVB and VIS arms

One-dimensional object and sky spectra are extracted from the 2D spectra. The sky spectrum is extracted from regions with the lowest continuum and nebular line emission. In the nights with four consecutive exposures, cosmic rays have been removed by taking the median value of each pixel in the four exposures. The sky spectra are subtracted from the object spectra, thereby correcting for the contamination by moonlight as well. After applying the barycentric correction, the sky-corrected object spectra of the three nights have been combined. Table 3 gives the signal-to-noise ratio (S/N) per resolution element of the result of each night and of the combined spectrum. For the stellar line analysis, we normalized the spectrum. Independently, we also calibrated the flux of the UVB and VIS spectra with standard star BD+17° 4708 (sdF8) taken on 2009 September 27, since there were no appropriate flux standard observations for each individual night. We did not correct the spectrum for slit losses.

2.1.2 NIR arm

We reduced the NIR spectra following the pipeline cascade for nodding mode up to extracted 1D spectra, and we combined the three nights. A telluric standard star (HD 4670, B9V) is used to correct for the telluric absorption features in the combined NIR spectrum, and to calibrate the relative flux. The NIR spectrum is scaled to match the absolutely calibrated VIS spectrum. The S/N of the combined NIR spectrum of all three nights is $\sim$3 in the J band, and $<$1 in the H and K bands. This is too low to detect stellar or nebular features in the spectrum; however, the level of the continuum can be retrieved by binning the flux in the atmospheric bands. The result is shown in Fig. 2.

2.2 The nebular emission spectra

The 2D spectra of each night are combined using the median value. We flux calibrate the combined 2D spectra with the same photometric standard star as we used for the object spectrum. Following the trace of C1_31, we extract 20 sub-apertures from each night's combined 2D spectrum, resulting in a set of 1D nebular spectra that are spatially separated by 0.75 arcsec each.[1] Independently, we apply this combining and sub-aperture extraction procedure as well to the non-flat-fielded 2D spectra, now using the sum. This allows us to determine the number of photons N, and thus the photon noise error $\sqrt{N}$ for every emission line in the nebular spectra. These errors are propagated in the values of the nebular properties described in Section 4.

3 ANALYSIS: THE C1_31 STELLAR SPECTRUM

Fig. 2 shows the combined flux-calibrated stellar spectrum of C1_31. The extinction-corrected flux should show a Rayleigh–Jeans wavelength dependence ($F_\lambda \propto \lambda^{-4}$), because we expect an early-type star based on the classification in Castro et al. (2008). To lift the observed spectrum to the slope of the scaled Kurucz model of a B0 star, we need to de-redden our spectrum with $A_{V,\rm star} = 2.3 \pm 0.1$, adopting $R_V = 3.24$ (Gieren et al. 2008). We apply the parametrized extinction law of Cardelli, Clayton & Mathis (1989). As a check, we do the same exercise by varying both R_V and $A_{V,\rm star}$. With $3.0 \lesssim R_V \lesssim 3.5$, the spectrum can be de-reddened to the intrinsic $F_\lambda \propto \lambda^{-4}$ slope with an $A_{V,\rm star} = 2.3 \pm 0.1$. With R_V outside this range, the de-reddened spectrum does not match the models for any value of $A_{V,\rm star}$.

Castro et al. (2008) report magnitudes $V = 18.523$ and $I = 19.239$ for NGC 55 C1_31, which were obtained as part of the Araucaria Cepheid search project (Pietrzyński et al. 2006). The I magnitude is in good agreement with our flux-calibrated spectrum; V is not. The reported colour $V - I = -0.716$ is even bluer than a theoretical Rayleigh–Jeans tail, suggesting a problem with the photometry.[2] From our flux-calibrated spectrum we obtain $V \simeq 20.1 \pm 0.1$. Using $A_{V,\rm star} = 2.3$ and $d = 2.0$ Mpc, we derive an absolute magnitude of $M_V = -8.7 \pm 0.4$ for the source.

Fig. 3 compares the observed UVB spectrum of C1_31 between 380 and 490 nm with that of spectral standard stars (Walborn & Fitzpatrick 1990). In the C1_31 spectrum, the Balmer and He I lines show artefacts of the nebular emission correction. However, most of the line wings are left unaffected thanks to the relatively high spectral resolution of X-shooter. Based on the non-detection of He II λ4541 and the presence of He I λ4471 in the C1_31 spectrum, one cannot classify this source as an early O star. By adding artificial noise to the standard star spectra, matching the S/N of our observations in this range, we estimate that the He II λ4541 line of a star with spectral type later than O7.5 will not be detectable, thus suggesting a late spectral subtype. In Section 3.1.1 we will use stellar atmosphere models to constrain the effective temperature more quantitatively. Supergiants may have strong emission in He II λ4686 due to their stellar wind, but none of the standard stars shows a feature as broad as that in our observations. Broad He II λ4686 emission lines are the strongest features in Wolf–Rayet (WR) stars of type WN. This line profile will be analysed in more detail in Section 3.1.4.

When we compare X-shooter spectrum to the FORS2 spectrum of C1_31 in Castro et al. (2008), we conclude that the

[1] The sub-aperture size of 0.75 arcsec is just below the average full width at half-maximum (FWHM) of the seeing.

[2] This has been confirmed by the authors. Corrected photometric values are $V = 19.87 \pm 0.05$, $I = 19.25 \pm 0.05$ (Pietrzyński, private communication), in agreement with our findings.

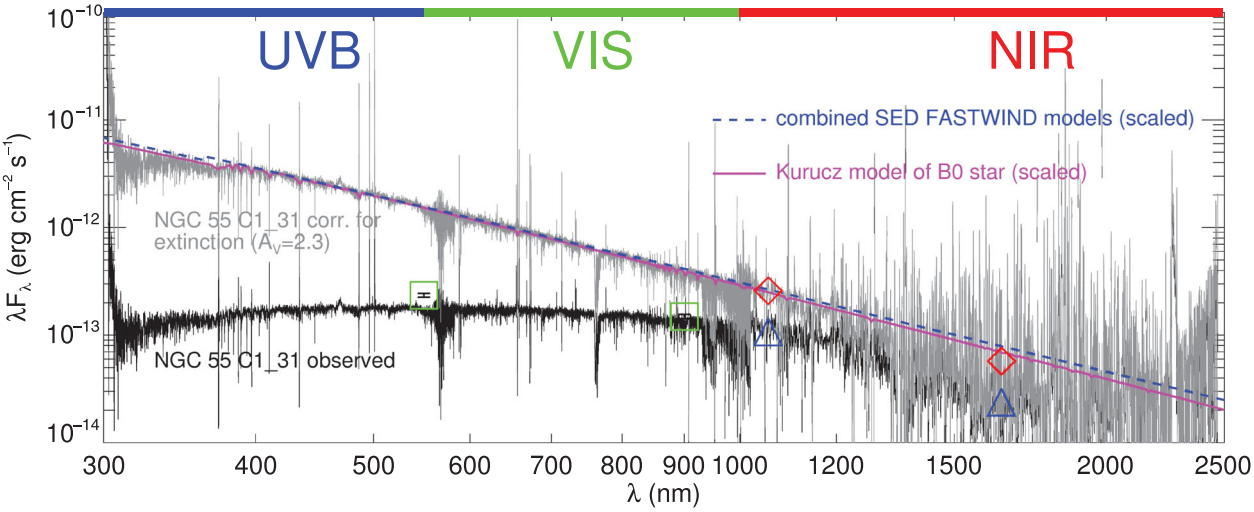

Figure 2. Flux-calibrated spectrum of NGC55 C1_31 (bottom), and the same spectrum (top) corrected for extinction with $R_V = 3.24$ and $A_{V,\mathrm{star}} = 2.3$ (see text). The dashed line shows the FASTWIND spectral energy distribution for the best-fitting combination of models (see Section 6); the solid line is a Kurucz model of a B0 star (Kurucz 1979, 1993). The ranges of X-shooters instrument arms are indicated at the top of the graph. The open squares point to the updated *V* and *I* magnitudes (Pietrzyński, private communication). For clarity, the NIR spectrum is shown here with a smoothing of seven points. The triangles show the integrated values of the observed flux in the *J* and *H* bands; the diamonds show their extinction-corrected values.

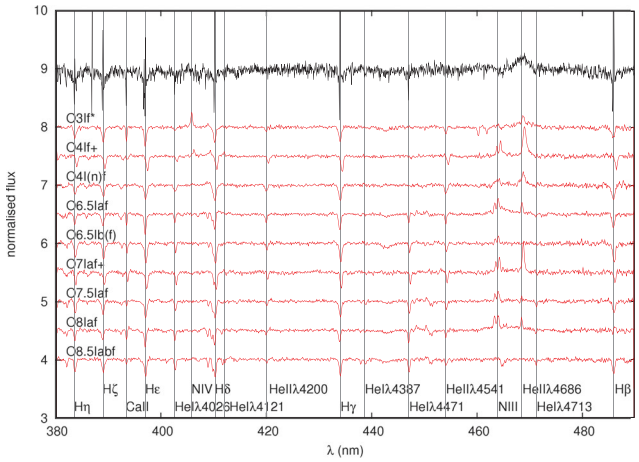

Figure 3. The normalized sky-corrected object spectrum (top) between 380 and 490 nm compared with the spectra of standard O supergiants from O3 to O8.5 (Walborn & Fitzpatrick 1990). Note the very broad He II λ4686 emission.

general appearance is similar, including the shape of He II λ4686. Castro et al. observed He II λ4200 weakly in emission as well; this we cannot confirm. The FORS2 observations will have suffered from similar nebular contamination in the Balmer lines as well as in some He I lines, which may have hampered earlier classification, but correcting for this is even more difficult at lower spectral resolution.

3.1 Stellar line profile modelling

Although we are going to make clear in this paper that C1_31 is very likely a composite source, we first approach the spectrum as if it is produced by a single star. The derived physical parameters therefore represent averages of the flux-weighted components contributing to the spectrum. We note, though, that the integrated light from clusters – in particular the hydrogen ionizing radiation – is often dominated by only a few of the most massive components.

The profiles of spectral lines are responsive to various stellar parameters such as effective temperature, mass-loss rate, surface gravity, chemical abundances and rotation speed. We have used FASTWIND (Puls et al. 2005) to model stellar atmospheres and to compute profiles of spectral lines. FASTWIND calculates non-local thermodynamic equilibrium (non-LTE) line-blanketed stellar atmospheres and is suited to model stars with strong winds. We first tried to apply a genetic fitting algorithm with FASTWIND models (see Mokiem et al. 2005) to the observed spectrum, in order to fit a large number of parameters at the same time. This did not result in well-constrained parameters, because the shape and width of He II λ4686 could not be fitted at the same time as the other lines.

Instead, we constructed a grid of FASTWIND models, and constrained the parameters by comparing the observed profiles with the models. The main grid varies effective temperature $T_{\mathrm{eff}} = 27\,500 - 35\,000$ K with steps of 2500 K, and covers values for the mass-loss rate $\dot{M} = 1$, 3, 6 and $10 \times 10^{-6}\,\mathrm{M_\odot\ yr^{-1}}$ and luminosity $\log(L_*/\mathrm{L_\odot}) = 5.4$, 5.6 and 5.8. All models have a mass of $M = 40\,\mathrm{M_\odot}$, wind acceleration parameter $\beta = 1.0$, and helium to hydrogen number density $N_{\mathrm{He}}/N_{\mathrm{H}} = 0.1$. Radius R_* and surface gravity g are fixed by the other parameters. The terminal wind velocity v_∞ is assumed to be 2.6 times the surface escape velocity (see Lamers, Snow & Lindholm 1995). In Table 4 we show the parameter values of a subset of the grid, i.e. the models discussed in more detail in this paper. Unless stated otherwise, the synthesized line profiles are produced using a microturbulent velocity of $v_{\mathrm{turb}} = 10\,\mathrm{km\,s^{-1}}$ and a projected rotational velocity of $v_{\mathrm{rot}}\sin(i) = 150\,\mathrm{km\,s^{-1}}$, with i being the inclination of the stellar rotation axis relative to the line of sight. An instrumental profile matching the resolution of X-shooter is applied as well.

We first investigate the overall impact of the effective temperature (Section 3.1.1), rotational velocity (Section 3.1.2) and mass-loss rate (Section 3.1.3) by comparing with models involving a single star. In Section 3.1.4 we show that the observed profile of He II λ4686 cannot be reproduced with a single star. In Section 3.1.5 we will discuss the luminosity constraint that follows from M_V.

Table 4. Parameters used for the described FASTWIND models, which are a subset of a larger grid. R_*, $\log g$ and $v_\infty = 2.6 \times v_{\rm esc}$ depend on the other variables. The first four models have the same M, L_* and $\dot{M}$, but different $T_{\rm eff}$, causing the remaining parameters to be modified. The next three models are variations on MOD31, but with different values for $\dot{M}$. MOD69 is like MOD31, but with an artificially high wind acceleration parameter β. The last two models MOD89 and MOD90 provide the best-fitting multiple model configuration (in a visual flux ratio of ∼4:1). The bolometric luminosities L_* are chosen such that they reproduce the measured M_V with 10 times MOD89 and two times MOD90.

ID	M ($M_\odot$)	$T_{\rm eff}$ (K)	L_* ($L_\odot$)	$\log g$ (cm s^{-2})	R_* ($R_\odot$)	$\dot{M}$ ($M_\odot$ yr^{-1})	v_∞ (km s^{-1})	β	$N_{\rm He}/N_{\rm H}$	Z ($Z_\odot$)
MOD39	40	27 500	$10^{5.6}$	2.99	33.69	6.00×10^{-6}	1750.33	1.0	0.1	0.3
MOD31	40	30 000	$10^{5.6}$	3.30	23.40	6.00×10^{-6}	2100.40	1.0	0.1	0.3
MOD32	40	32 500	$10^{5.6}$	3.44	29.94	6.00×10^{-6}	2275.43	1.0	0.1	0.3
MOD33	40	35 000	$10^{5.6}$	3.57	17.19	6.00×10^{-6}	2450.47	1.0	0.1	0.3
MOD10	40	30 000	$10^{5.6}$	3.30	23.40	1.00×10^{-6}	2100.40	1.0	0.1	0.3
MOD11	40	30 000	$10^{5.6}$	3.30	23.40	3.00×10^{-6}	2100.40	1.0	0.1	0.3
MOD12	40	30 000	$10^{5.6}$	3.30	23.40	1.00×10^{-5}	2100.40	1.0	0.1	0.3
MOD69	40	30 000	$10^{5.6}$	3.30	23.40	6.00×10^{-6}	2100.40	3.0	0.1	0.3
MOD89	30	30 000	$10^{5.24}$	3.54	15.46	2.00×10^{-6}	2237.86	1.0	0.1	0.3
MOD90	80	50 000	$10^{5.83}$	4.26	10.98	3.00×10^{-5}	4336.76	1.0	0.8	0.3

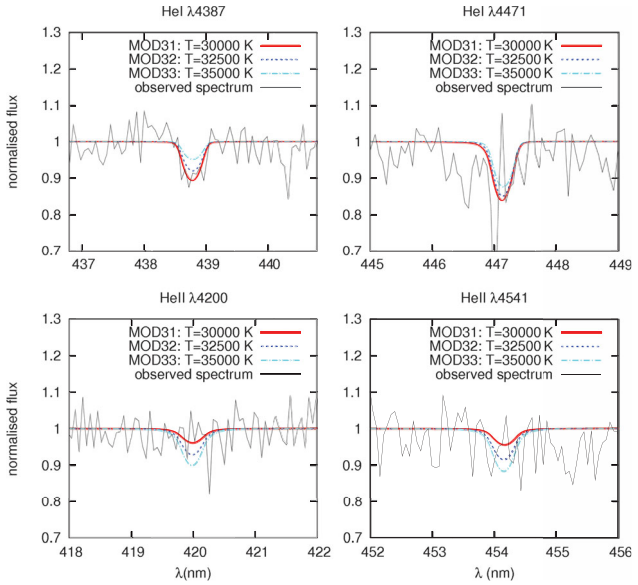

Figure 4. Observed line profiles compared with model line profiles computed for various effective surface temperatures (see text).

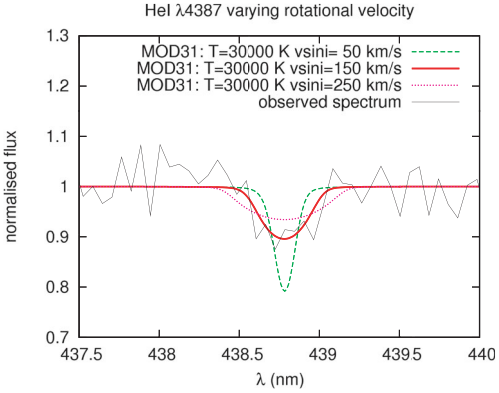

Figure 5. The observed line profile of He I λ4387 compared with the same model profile as computed for various projected rotational velocities.

3.1.1 *Effective temperature*

The He I and He II lines can be used to determine the characteristic effective temperature of the source. Fig. 4 shows the observed profiles of He I λ4387, He I λ4471, He II λ4200 and He II λ4541 along with profiles from atmosphere models that only differ in effective temperature. A visual comparison of the profiles shows that the models with $T_{\rm eff} < 35\,000$ K best reproduce the spectrum as otherwise He II would have been detected, and He I λ4387 would not have been as deep.

3.1.2 *Rotational velocity*

Since the observed profile of He I λ4387 is not affected by nebular emission, we can use it to constrain the characteristic rotational broadening. Fig. 5 shows the He I λ4387 profile of MOD31 ($T_{\rm eff} = 30\,000$ K) convolved with rotational profiles to simulate three different rotational velocities: $v_{\rm rot}\sin(i) = 50$, 150 and 250 km s^{-1}. The line with $v_{\rm rot}\sin(i) = 50$ kms^{-1} is clearly not broad enough to fit the observed profile, while the line with $v_{\rm rot}\sin(i) = 250$ kms^{-1} appears to be too broad. We conclude that the width of the lines is best reproduced by models with $v_{\rm rot}\sin(i) = 150 \pm 50$ km s^{-1}.

3.1.3 *Mass-loss rate*

In the nebular spectrum, Hα is very strongly in emission. This is mostly due to the surrounding H II region. In the sky-corrected object spectrum (Fig. 6), the Hα line wings are clearly visible, and reveal that Hα is in emission in the spectrum of C1_31 as well.

The profile of Hα is very sensitive to the mass-loss flux $\dot{M}/4\pi R_*^2$. In the right-hand panel of Fig. 6 we plot the observed spectrum together with the line profiles from single-star models with $T_{\rm eff} = 30\,000$ K and $R_* = 23.4\,R_\odot$, and four different mass-loss rates: 1×10^{-5}, 6×10^{-6}, 3×10^{-6} and $1 \times 10^{-6}\,M_\odot$ yr^{-1}. Depending on the mass-loss rate, the line is either in emission or in absorption. The computed profile for MOD31 reproduces the observed profile best, and corresponds to a mass-loss flux close to $\sim 9 \times 10^{-10}\,M_\odot$ yr$^{-1}\,R_\odot^{-2}$ (i.e. $\dot{M} = 6 \times 10^{-6}\,M_\odot$ yr^{-1} for $R_* = 23.4\,R_\odot$).

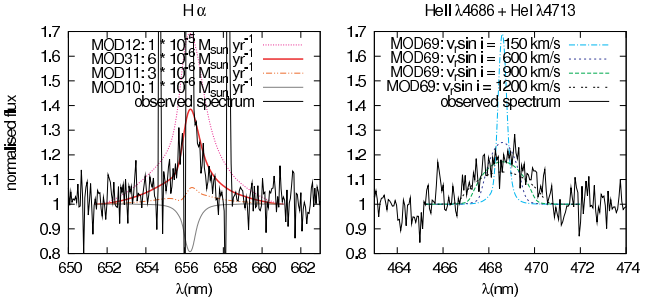

Figure 6. Observed line profiles compared with model line profiles for various mass-loss rates (left-hand panel) and projected rotational velocities (right-hand panel).

3.1.4 He II λ4686

In the spectrum of C1_31, He II λ4686 is in emission, which is a common feature in spectra of O-type supergiants (see Fig. 3). However, in none of the comparison spectra this line is as broad as in our spectrum ($\sim$3000 km s^{-1}). The equivalent width is only -3.6 ± 0.04 Å, i.e. much weaker than in typical WN star spectra. The feature is of stellar origin as no nebular counterpart is detected.

The strength of He II λ4686 depends on various parameters in the FASTWIND models. The modelled line can be made stronger by (1) increasing the effective temperature (a larger fraction of the helium will be ionized), (2) increasing the mass-loss rate, (3) increasing the helium abundance, (4) increasing the wind acceleration parameter β or (4) decreasing the terminal wind velocity. But these modifications only make the line stronger, not much broader. To simulate the profile of the line in both strength and width using rotational broadening, a rotational velocity of $v_{\rm rot}\sin(i) = 1200\,{\rm km\,s^{-1}}$ is needed. Fig. 6 shows one of the models (MOD69) for which this line has an equivalent width of -3.58 Å, convolved with a rotational profile simulating rotational velocities of $v_{\rm rot}\sin(i) = 150$, 600, 900 and 1200 km s^{-1}. Only when $v_{\rm rot}\sin(i) \sim 1200\,{\rm km\,s^{-1}}$, the line is broad enough to reproduce the observed profile. This $v_{\rm rot}$ is, for acceptable radii and masses, higher than the escape velocity. He II λ4686 is formed in the wind; therefore, its width can be much higher than the surface rotational velocity. But with such a dense and fast wind, Hα would have been much broader as well, and the photospheric He I and He II absorption lines would not be visible. Therefore, we conclude that the He II λ4686 emission line has a different origin: it is a diluted WN feature (see Section 6).

3.1.5 Luminosity

In the calibration of O stars by Martins, Schaerer & Hillier (2005) the visually brightest supergiant has $M_V = -6.35$. C1_31 is with $M_V = -8.7$ almost an order of magnitude brighter. It is therefore likely that C1_31 is a composite object such as a cluster containing several luminous stars. The slit width (0.8 arcsec for UVB) at a distance of 2.0 Mpc corresponds to a physical size of 7.8 pc, which is large enough to contain for example the Orion Trapezium cluster, or even more massive open clusters such as Tr 14 (Sana et al. 2010) or NGC 6231 (Sana et al. 2008).

In summary, the normalized line profiles of hydrogen and helium, except He II λ4686, can be reproduced by a single-star model with parameters $T_{\rm eff} \sim 30\,000$ K and $\dot{M} \sim 6 \times 10^{-6}\,{\rm M_\odot\,yr^{-1}}$, $R_* \sim 23.4\,{\rm R_\odot}$ and $v_{\rm rot}\sin(i) = 150 \pm 50\,{\rm km\,s^{-1}}$, i.e. a late O supergiant star (MOD31 in Table 4). A star with this temperature would need a luminosity of $\log(L_*/L_\odot) \sim 6.3$ to reproduce M_V, which is too high for a single O-type supergiant. The considerations regarding the He II λ4686 line also point in the direction of the spectrum being a composite of different sources, weighed by their visual brightness. This scenario will be explored in Section 6.

Table 5. Reddening-corrected (see text) line flux ratios with respect to Hβ for the strongest unblended emission lines in the nebular spectrum close to our central source.

Line	2009 August 13 ratio	2009 September 27 ratio	Average ratio
[O II] λ3726	1.554 ± 0.050	1.476 ± 0.033	1.500 ± 0.028
[O II] λ3729	2.271 ± 0.065	2.188 ± 0.044	2.214 ± 0.036
H-9 λ3835	0.062 ± 0.011	0.060 ± 0.007	0.061 ± 0.006
[Ne III] λ3869	0.325 ± 0.018	0.306 ± 0.012	0.312 ± 0.010
H-8 λ3889	0.201 ± 0.014	0.198 ± 0.009	0.199 ± 0.008
Hδ λ4102	0.275 ± 0.014	0.271 ± 0.010	0.272 ± 0.008
Hγ λ4341	0.517 ± 0.019	0.505 ± 0.013	0.509 ± 0.011
[O III] λ4363	0.039 ± 0.004	0.037 ± 0.003	0.037 ± 0.002
He I λ4471	0.034 ± 0.005	0.034 ± 0.004	0.034 ± 0.003
He II λ4686	0.006 ± 0.002	0.003 ± 0.001	0.003 ± 0.001
Hβ λ4861	1.000 ± 0.027	1.000 ± 0.019	1.000 ± 0.016
[O III] λ4959	1.171 ± 0.029	1.144 ± 0.020	1.153 ± 0.016
[O III] λ5007	3.477 ± 0.074	3.426 ± 0.052	3.443 ± 0.043
He I λ5876	0.110 ± 0.007	0.113 ± 0.005	0.112 ± 0.004
[S III] λ6312	0.015 ± 0.002	0.017 ± 0.001	0.016 ± 0.001
[N II] λ6548	0.060 ± 0.004	0.062 ± 0.003	0.061 ± 0.002
Hα λ6563	3.040 ± 0.063	3.052 ± 0.045	3.048 ± 0.037
[N II] λ6583	0.179 ± 0.007	0.193 ± 0.005	0.188 ± 0.004
He I λ6678	0.029 ± 0.003	0.028 ± 0.002	0.028 ± 0.002
[S II] λ6716	0.269 ± 0.009	0.292 ± 0.007	0.283 ± 0.005
[S II] λ6731	0.189 ± 0.007	0.206 ± 0.005	0.200 ± 0.004
[Ar V] λ7006	0.009 ± 0.001	0.006 ± 0.001	0.007 ± 0.001
[Ar III] λ7136	0.087 ± 0.004	0.086 ± 0.003	0.087 ± 0.002
[Ar III] λ7751	0.022 ± 0.001	0.022 ± 0.001	0.022 ± 0.001
Pa-10 λ9015	0.017 ± 0.001	0.018 ± 0.001	0.018 ± 0.001
[S III] λ9069	0.200 ± 0.005	0.203 ± 0.004	0.202 ± 0.003
Pa-9 λ9230	0.025 ± 0.002	0.024 ± 0.001	0.024 ± 0.001
[S III] λ9531	0.475 ± 0.011	0.437 ± 0.008	0.449 ± 0.006
Pa-7 λ10050	0.045 ± 0.004	0.046 ± 0.003	0.046 ± 0.002

4 ANALYSIS: THE NEBULAR EMISSION-LINE SPECTRUM

The nebular emission spectra show hydrogen recombination lines of the Balmer and Paschen series, He I lines, and forbidden lines of O II, O III, S II, S III, N II, Ne III, Ar III, Ar IV and Ar V. To these spectra, no sky correction could be applied, because nebular emission covers the full slit. Therefore, every nebular line we measure might have a contribution from the sky continuum. We minimize this error by subtracting the local continuum next to the line in wavelength. The ratios with respect to Hβ of the nebular lines at the position of our source are listed in Table 5. The extinction-corrected integrated specific intensity of Hβ is 5.8×10^{-15} erg s^{-1} cm^{-2} arcsec^{-2}.

We use the diagnostics for electron temperature and oxygen abundance from Pagel et al. (1992):

$$T = \frac{1.432}{\log R - 0.85 + 0.03\log T + \log\left(1 + 0.0433x\,T^{0.06}\right)}, \quad (1)$$

where $T \equiv T$ (O III), the electron temperature in the region where oxygen is doubly ionized, in units of 10^4 K. R and x are given by

$$R = \frac{I_{\lambda4959} + I_{\lambda5007}}{I_{\lambda4363}}, \quad (2)$$

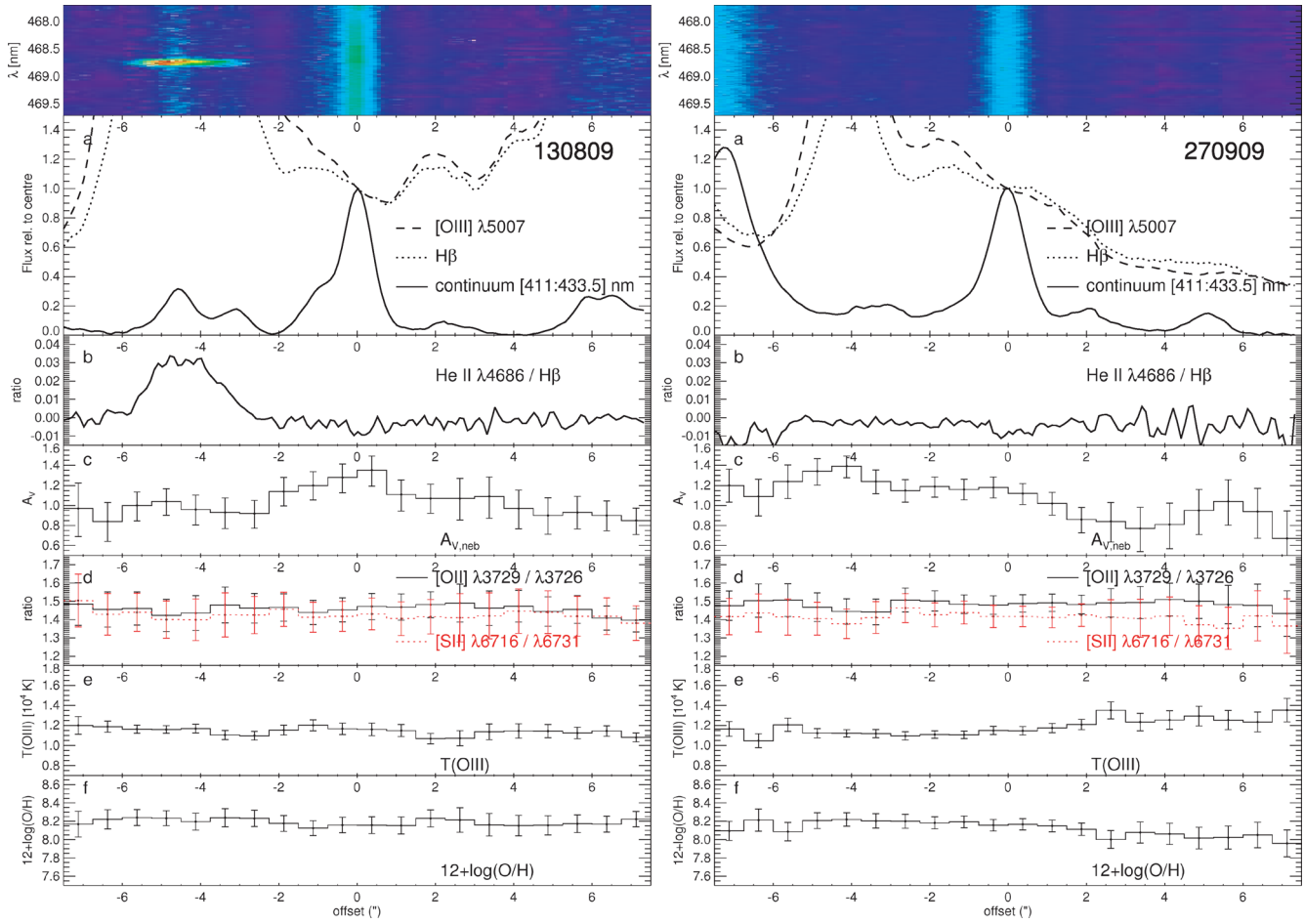

Figure 7. Spatial profiles of emission lines and properties measured from the emission-line spectrum in 20 sub-apertures along the slit. On the x-axis is distance in arcsec from C1_31. The left and right frames, labelled by their observing dates, correspond to observations with different slit orientations (see Fig. 1 and Table 1). The image at the top is a part of the 2D spectrum around 468.6 nm. Panel (a) shows the average level of the continuum between 411.0 and 433.5 nm, without taking into account the difference in $A_{V,\mathrm{neb}}$ along the slit. It also shows the intensity of the two strong nebular lines Hβ and [O III] λ5007, with respect to the value at the location of the central source. Panel (b) shows the flux of the He II λ4686 nebular emission line with respect to Hβ. Panel (c) shows the value of $A_{V,\mathrm{neb}}$, derived from a number of Balmer and Paschen emission lines, assuming case B recombination. Panel (d) shows [O II] and [S II] ratios that are sensitive to electron density. Panel (e) shows T (O III) calculated from the ratio R of the [O III] lines (equation 1). Panel (f) shows the total oxygen abundance $12 + \log(\mathrm{O/H})$.

$$x = 10^{-4} n_\mathrm{e} T_2^{-1/2}, \tag{3}$$

where I is the integrated specific intensity of the indicated emission line and n_e is the electron density in cm^{-3}. T_2 is the electron temperature in units of 10^4 K in the singly ionized region, and follows from model calculations by Stasińska (1990):

$$T_2^{-1} \equiv [T(\mathrm{O\,II}, \mathrm{N\,II}, \mathrm{S\,II})]^{-1} = 0.5\left(T^{-1} + 0.8\right). \tag{4}$$

The mean ionic abundance ratios for O II and O III along the line of sight are calculated as follows:

$$12 + \log(\mathrm{O\,II}/\mathrm{H\,II}) = \log\frac{I_{\lambda3726} + I_{\lambda3729}}{I_{\mathrm{H}\beta}} + 5.890 + \frac{1.676}{T_2} - 0.40\log T_2 + \log(1 + 1.35x), \tag{5}$$

$$12 + \log(\mathrm{O\,III}/\mathrm{H\,II}) = \log\frac{I_{\lambda4959} + I_{\lambda5007}}{I_{\mathrm{H}\beta}} + 6.174 + \frac{1.251}{T} - 0.55\log T. \tag{6}$$

The total oxygen abundance is obtained by adding equations (5) and (6), i.e. by assuming these two ionization stages to be dominant in the H II region.

4.1 Nebular emission properties along the slit

Fig. 7 shows the nebular properties along the slit for the spectra obtained on 2009 August 13 and September 27. The orientation of the slit differs between these observations: positive offset is approximately north-east for 2009 August 13 and north-west for September 27 (see Fig. 1). We do not show the results for the 2009 September 30 observation, which has a similar position angle and gives a similar result as to the 2009 September 27 observation, though with larger error bars. As mentioned in Section 2.2, the errors are obtained by propagating the photon noise on the intensity of the used lines. We choose $n_\mathrm{e} = 20\,\mathrm{cm}^{-3}$ arbitrarily, but in agreement with the low density limit of the density-sensitive [O II] and [S II] ratios we measure (see Fig. 7d and the analysis below). The error on the density is not propagated into the errors on the other parameters, because they all depend very weakly on the density (see equations 1 and 3). In the following sections, we discuss the panels of Fig. 7.

4.1.1 Stellar continuum and nebular emission

Fig. 7(a) shows the shape of the continuum between 411.0 and 433.5 nm; here we see the trace of our central source. We do not

take into account the difference in $A_{V,\mathrm{neb}}$ along the slit (see Fig. 7c). The nebular emission in Hβ and [O III] λ5007, two of the strongest emission lines in the spectra, is also shown. [O III] λ5007 is a forbidden transition and thus only emitted by low-density nebulae. The 2009 September 27 observation suggests that the nebular emission is built up from various discrete peaks, of which one is centred on C1_31. This part of the nebula, with a radius of ∼20–30 pc, is likely ionized by C1_31. Therefore, the nebular properties at the central location in the slit are related to the properties of C1_31 (see Section 5).

4.1.2 He II λ4686 / Hβ

Fig. 7(b) shows the ratio of the He II λ4686 and Hβ nebular emission line. Around C1_31, this nebular line is not present, but it is very pronounced in the 2009 August 13 spectrum around an offset of −4.5 arcsec. This is also clearly visible in the 2D spectrum around this line (the top left image of Fig. 7). This feature will be discussed in more detail in Section 4.2. This nebular feature is much narrower than the wind He II λ4686 line we discussed in Section 3.1.4. The nebular He II λ4686 line has a Gaussian FWHM of ∼1 Å like the other nebular lines, slightly larger than the resolution element at this wavelength (∼0.75 Å).

4.1.3 Extinction

Fig. 7(c) shows the values of $A_{V,\mathrm{neb}}$, which is the extinction derived from the nebular hydrogen line ratios. Adopting $R_V = 3.24$ (Gieren et al. 2008), $A_{V,\mathrm{neb}}$ is found for each aperture by minimizing the following expression:

$$\chi^2_{\mathrm{red}} = \frac{\chi^2}{\nu} = \frac{1}{\nu} \sum_{\mathrm{lines}} \frac{(q - q_0)^2}{\sigma_q^2}, \tag{7}$$

where q_0 is the theoretical ratio for case B recombination in the low density limit at $T = 10\,000$ K (see e.g. Osterbrock & Ferland 2006), q is the intensity of a line with respect to Hβ after applying $A_{V,\mathrm{neb}}$ (following Cardelli et al. 1989), σ_q^2 is the variance on q, and ν is the number of degrees of freedom. We use H-9, Hγ, Hδ, Hα, Pa-10, Pa-9 and Pa-7. The confidence interval on $A_{V,\mathrm{neb}}$ is given by the value for which χ^2_{red} rises by 1. $A_{V,\mathrm{neb}}$ is used in the derivation of the properties per aperture shown in Figs 7(e) and (f); the error on $A_{V,\mathrm{neb}}$ is not propagated as its influence on the other parameters is small.

$A_{V,\mathrm{neb}}$ at the location of C1_31 is derived to be 1.30 ± 0.15 and 1.15 ± 0.10 in the 2009 August 13 and September 27 spectra, respectively. This is lower than $A_{V,\mathrm{star}} = 2.3 \pm 0.1$ (see Section 3 and Fig. 2). Furthermore, we note that both $A_{V,\mathrm{neb}}$ and $A_{V,\mathrm{star}}$ are larger than $A_V = 0.45$ from Gieren et al. (2008). However, the latter value is an average for NGC 55 as a whole. This range of values reflects local variations and are to be expected, especially in an almost edge-on galaxy.

4.1.4 Electron density

Fig. 7(d) shows [O II] and [S II] ratios that are sensitive to electron density (see e.g. Osterbrock & Ferland 2006). For a value of >1.4, both ratios are in the low density ($<10^2$ cm^{-3}) limit, so this measurement only provides an upper limit. Because these line pairs are very close in wavelength, their ratios are not affected by $A_{V,\mathrm{neb}}$.

4.1.5 Electron temperature

Fig. 7(e) gives the electron temperature calculated from the ratio R of the [O III] lines (equation 1). In the 2009 September 27 observation (Fig. 7, right) in the apertures with an offset of > 2 arcsec, [O III] λ4363 was hardly detected, resulting in an underestimation of the error in T (O III). Taking this into account, and weighing the better quality spectra more strongly, we conclude that around the location of C1_31 T (O III) = 11500 ± 600 K, and that there are no significant gradients in the two spatial directions indicated in Fig. 1.

4.1.6 Oxygen abundance

Fig. 7(f) shows the total oxygen abundance [O/H] = 12 + log (O/H). The slight drop in [O/H] that we see at an offset of >2 arcsec in the 2009 September 27 observation is a propagated effect from the uncertain determination of T (O III). Excluding this region, we find an average of [O/H] = 8.18 ± 0.03, which corresponds to $Z = 0.31 \pm 0.04\,Z_\odot$ adopting $[\mathrm{O/H}]_\odot = 8.69 \pm 0.05$ (Asplund et al. 2009). Though lower oxygen abundances are reported for NGC 55 (8.08 ± 0.10; Tüllmann et al. 2003), on average slightly higher values are measured (8.23–8.39, Webster & Smith 1983; 8.53, Stasińska et al. 1986; 8.35 ± 0.07, Zaritsky et al. 1994).

4.2 C2_35

C2_35 (RA 0:14:59.68, Dec. −39:12:42.84) is located 4.5 arcsec west–south-west of C1_31 (see Fig. 1). Its strongly ionized surrounding nebula is visible in the 2009 August 13 spectrum (Fig. 7a, left panel). At an offset of −4.5 arcsec we see a weak continuum, as the point-spread function of C2_35 is mostly outside the slit. We detect strong (forbidden) nebular line emission (panel a), but the most striking feature is the high He II λ4686 / Hβ = 0.03 ratio (left, panel b and top image). The FORS2 spectrum of C2_35, classified as an early O I by Castro et al. (2008), is similar to C1_31. The broad He II λ4686 wind feature is indicative of the presence of a hot WR star. On top of the broad wind feature, there is a narrow nebular emission line. He II emission lines from nebulae are only rarely seen and often associated with strong X-ray sources (e.g. Pakull & Angebault 1986; Kaaret, Ward & Zezas 2004) but see Shirazi & Brinchmann (2012). No obvious X-ray source is detected in archival *XMM–Newton* and *Chandra* observations at the location of C2_35 (R. Wijnands, private communication). The exposure times of these images, however, would not be sufficient to detect the X-ray emission of, for example, an accreting stellar mass black hole at this distance.

5 MODEL H II REGION

If the stellar spectrum is a composition of different sources, various solutions are possible. However, the properties T(O III), n_e and [O/H] of the surrounding nebula are constrained (see Section 4), and the nebular emission profiles along the slit give some idea of the size of the ionized region. The ionizing source, of which the constituents are constrained by the stellar spectrum, should be able to produce a region with properties we derive from the nebular spectrum. In this section, we will use the spectral synthesis code CLOUDY (version 08.00; Ferland et al. 1998) to investigate which properties of the nebula and of the central ionizing source have a strong influence on the observables that we measured. This will allow us to constrain T_{eff} and L_* of the ionizing source.

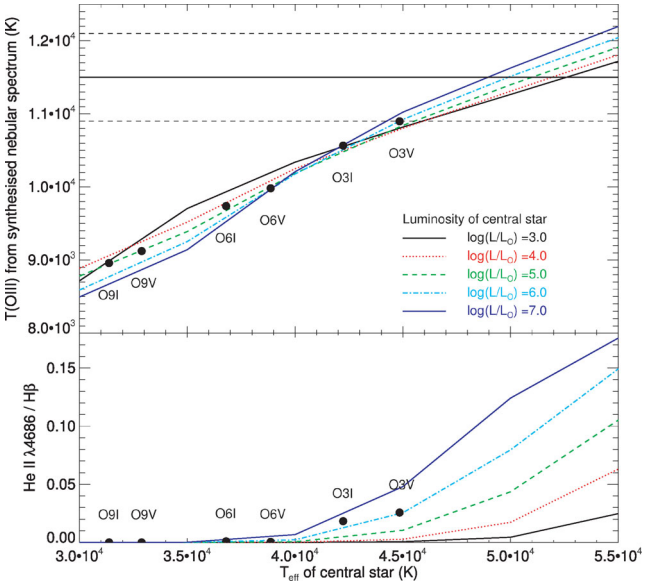

Figure 8. Upper panel: the predicted T(O III) from the synthesized nebular spectrum as a function of $T_{\rm eff}$ and L_* of a central ionizing O star (Lanz & Hubeny 2003) in a CLOUDY model with an inner radius of 0.1 pc. The solid and dashed horizontal lines are the observed T(O III) and error estimate for the direct environment of C1_31. Lower panel: the predicted nebular line ratio He II λ 4686/Hβ as a function of $T_{\rm eff}$ and L_* of a central ionizing star. The black dots correspond to realistic dwarf and supergiant O-type stars in the $T_{\rm eff}$ and L_* grid (Martins et al. 2005).

CLOUDY is designed to simulate gaseous interstellar media. From a given set of conditions such as luminosity and spectral shape of the ionizing source, the program computes the thermal, ionization and chemical structure of a region as well as the emitted spectrum. In order to compare our model results to what has been observed, we will mainly use the simulated emitted spectrum. Since we only know the total abundance of oxygen, we use the abundance pattern corresponding to the Orion nebula provided by CLOUDY (Baldwin et al. 1991; Rubin et al. 1991; Osterbrock, Tran & Veilleux 1992; Savage & Sembach 1996), and scale the metallicity such that the oxygen abundance matches our observed value. The total hydrogen density $n_{\rm H}$ is set to 20 cm^{-3}, consistent with the low electron density limit derived from [O II] and [S II], assuming that all hydrogen is ionized. We do not include dust grains.[3] We use a spherical geometry: the inner radius of the cloud is 0.1 pc and the outer radius is set where the temperature drops below 4000 K.

We examined the ratio R (equation 2) of the modelled output spectra, and computed T(O III), as a function of $T_{\rm eff}$ and L_* of a synthetic O-star spectrum (Lanz & Hubeny 2003) as central ionizing source; see the upper panel of Fig. 8. A grid of $T_{\rm eff}$ = 30 000–55 000 K and log (L/L$_\odot$) = 3–6 has been examined; the black dots indicate realistic stars in this grid according to the calibration of Martins et al. (2005). We see that a higher $T_{\rm eff}$ of the central star leads to a higher T(O III), while the effect of L_* on the 'measured' T(O III) is smaller. L_* does however influence the size of the cloud: a higher L_* leads to a larger cloud. A cloud with metallicity $Z = 0.3\,{\rm Z}_\odot$ needs a $T_{\rm eff} \sim 44\,000$–$55\,000$ K star, depending on the luminosity, to produce the measured T(O III) of 11 500 $\pm$ 600 K (horizontal line). Furthermore, we find that the metallicity of the cloud has an even stronger influence on T(O III); lower metallicities result in hotter clouds because they are less efficiently cooled. Changing $n_{\rm H}$ only influences the spatial scale of the cloud: a density 10 times as low results in a region four times as large.

We also analysed the nebular line ratio He II λ 4686/Hβ as a function of $T_{\rm eff}$ and L_* of a central ionizing source; see the lower panel of Fig. 8. Below $T_{\rm eff} \simeq 40\,000$ K, no significant He II λ 4686 line is predicted for any of the luminosities in our grid. For $T_{\rm eff} > 40\,000$ K, the line can be produced, and is stronger with respect to Hβ for more luminous sources. The ratio He II λ 4686/Hβ decreases strongly by increasing the inner radius of the model cloud. The nebula directly around C1_31 does not show He II λ 4686; therefore, the inner radius is likely to be 1 pc or more. T(O III) is not affected significantly by changing the inner radius.

6 DISCUSSION: A CONSISTENT PICTURE

In the previous sections, we have put constraints on the stellar parameters of C1_31 and its surrounding region. We suggest that C1_31 is not a single object, but rather a stellar cluster. We summarize the main arguments below.

(a) The line profiles cannot be reproduced by one single stellar atmosphere model, especially not He II λ4686 (Section 3.1.4).

(b) The visual absolute magnitude $M_V = -8.7$ of this source is very high for a single object (Section 3).

(c) A very hot central object (∼50 000 K) is necessary to produce a T(O III) of ∼11 500 K in the surrounding nebula (Section 5), but the 'average' spectral type suggests that the majority of the luminosity in the visual is produced by $T_{\rm eff} \lesssim 35\,000$ K stars (Section 3.1.1).

The spectrum of a composite object results in a superposition of all components, weighed by their relative brightness at the wavelength considered. All lines that we analysed are close in wavelength, so we adopt a general ratio in brightness which is the ratio in V. Given a universal initial mass function (IMF), a cluster will consist of many cool low-mass stars, and only a few very luminous and hot ones. In this analysis we will focus on the most massive and luminous members, because these dominate the cluster spectrum, as well as the flux of ionizing photons. To this end, we present a simple combination of FASTWIND models that (a) reproduces all observed line profiles, (b) has an absolute magnitude $M_V = -8.7$ and (c) when put into a CLOUDY model of an H II region, produces an electron temperature of T(O III) ∼11 500 K, for an adopted metallicity of $Z = 0.3\,{\rm Z}_\odot$ and hydrogen density $n_{\rm H} = 20\,{\rm cm}^{-3}$.

Model MOD90 (see Table 4) has a high temperature ($T_{\rm eff}$ = 50 000 K), a high mass-loss rate ($3 \times 10^{-5}\,{\rm M}_\odot\,{\rm yr}^{-1}$) and an enhanced helium abundance $N_{\rm He}/N_{\rm H} = 0.8$. It mimics a Wolf–Rayet WN star (see e.g. Crowther 2008). These properties result in a strong and broad He II λ4686 emission feature (Fig. 9, upper right). To reproduce the observed shape of He II λ4686, we combine this profile with a model with a weak He II λ4686 absorption profile: model MOD89, with $T_{\rm eff} = 30\,000$ K. This model resembles a late-O/early-B giant or bright giant. We create a combined profile of 20 per cent MOD90 and 80 per cent MOD89. With this flux ratio, the He I and He II absorption lines resemble a 30 000-K star, because in this respect the MOD89 model is dominant. The Hα wings are well reproduced (Fig. 9, upper right). The other Balmer lines in the WN

[3] We exclude dust grains to keep the model simple. The extinction we measure both in the stellar spectrum and the hydrogen emission lines could as well be due to dust that is outside the surrounding ionized region.

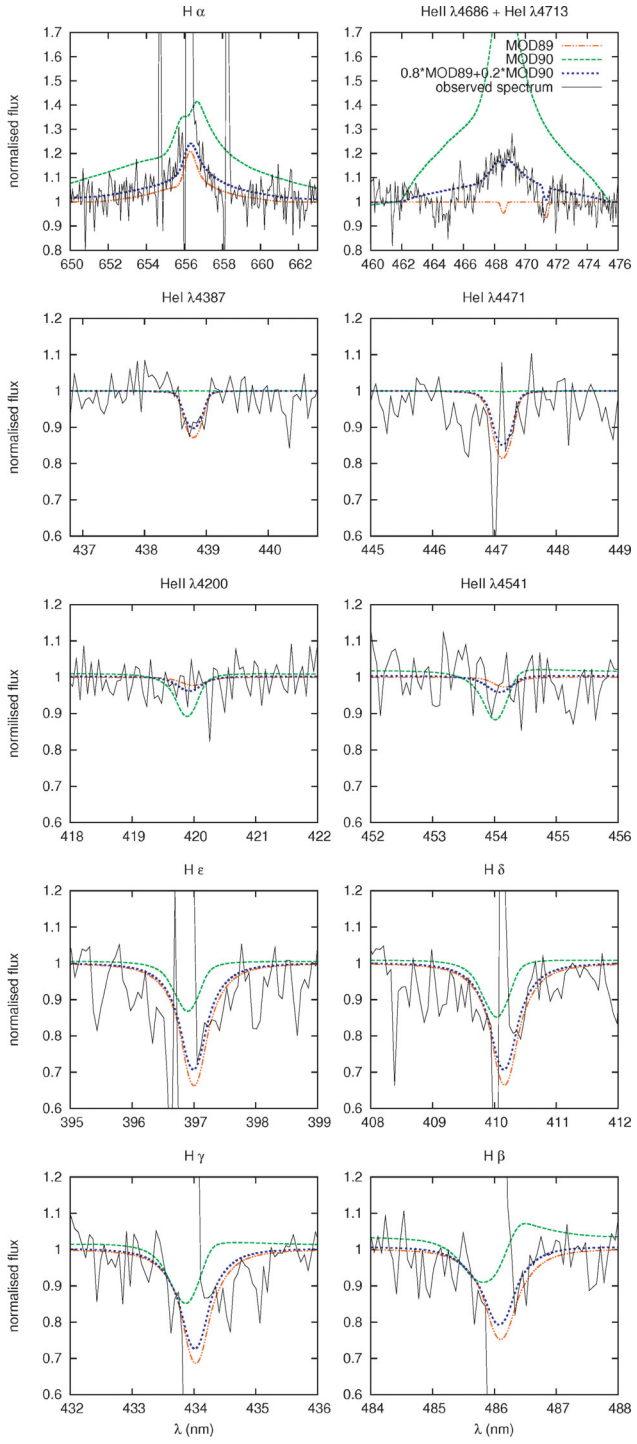

Figure 9. The observed normalized spectrum (solid lines) together with the combined line profiles (dotted lines) from the models described in Table 4, representing the late O giant component MOD89 (dash–dotted lines) and the WN-like component MOD90 (dashed lines), in the ratio 4:1.

component MOD90 are also affected by the strong wind, which results in a shallower line or even a P-Cygni profile in the case of Hβ and Hγ. However, the strong absorption profile of the late O giant component MOD89 dominates, and the combined profiles match the observed ones.

If the cluster consists of 10 stars like MOD89 and two like MOD90, the ensemble would have a visual magnitude of $M_V = -8.63$, in agreement with the observed value of $M_V = -8.7 \pm 0.4$. The flux ratio in the visual would be ∼4:1, due to the different bolometric corrections (see Table 6). The visual flux is dominated by the late O-type component, while further to the UV, the hot Wolf–Rayet component would dominate. The latter is required to reproduce the observed electron temperature in the cloud.

Table 6. Properties of the final composition of the cluster. Our model cluster has two different components: a late O giant component (MOD89) and a Wolf–Rayet WN-type component (MOD90) (see also Table 4). Column 1: model ID; column 2: effective temperature; column 3: bolometric luminosity; column 4: bolometric correction; column 5: absolute visual magnitude; column 6: number of stars of this type in the cluster; column 7: total absolute magnitude of this component and; column 8: fraction of the total visual flux provided by this component.

ID	$T_{\rm eff}$ (K)	L_* ($L_\odot$)	BC	M_V	No.	M_V total	Fraction of $F_{\rm vis}$
MOD89	30 000	$10^{5.24}$	−2.42	−5.93	10	−8.43	0.8
MOD90	50 000	$10^{5.83}$	−3.90	−5.95	2	−6.70	0.2

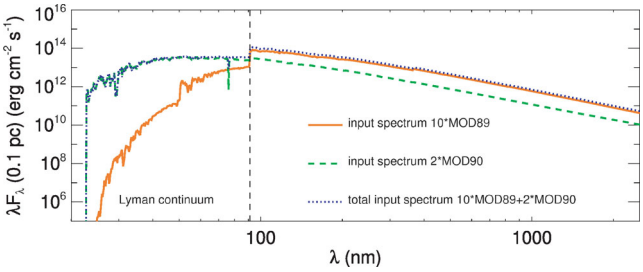

Figure 10. The spectral energy distribution at the inner radius of the model cloud ($r_{\rm in} = 0.1$ pc), split in the different components. It is clear that in the visual, the 30 000-K component (MOD89, dot–dashed lines) dominates the light, while the hydrogen ionizing photons (left of the vertical dashed line, with $h\nu > 13.6$ eV) are provided mainly by the hot (50 000 K) WN component (MOD90, dashed lines). The dotted profile shows the total input spectrum.

We have used the combined spectrum of 10 times MOD89 and two times MOD90 as ionizing source in a CLOUDY model. The spectral energy distribution at the inner radius of the cloud is shown in Fig. 10, where we see that the ionizing flux is indeed dominated by the WN component MOD90. We use the same configuration as we did in Section 5, with $Z = 0.3\,Z_\odot$. We choose $n_{\rm H} = 20\,{\rm cm}^{-3}$, such that CLOUDY produces an ionized region with a radius of ∼20 pc (see Section 4.1). From the synthesized nebular spectrum we infer T(O III) ∼10 800 K, slightly lower than the measured T(O III) ∼11 500 ± 600 K, but in reasonable agreement. According to the model in Section 5 and its results in Fig. 8, a 50 000-K star would be able to heat the cloud to ∼11 500 K. However, adding more late O stars decreases T(O III). The predicted nebular line ratio He II λ 4686/Hβ for this cluster composition is 0.06, which challenges the non-detection of nebular line He II λ 4686 around C1_31. This disagreement can be reconciled by increasing the inner radius of the model cloud to 1 pc or more.

In principle, information as to the stellar content may also be derived from considering the mass-loss rates of the contributing stars. For our late O II/III source (MOD89) the adopted mass-loss rate of $2 \times 10^{-6}\,{\rm M}_\odot\,{\rm yr}^{-1}$ is rather large compared to theoretical expectations for such a star at a metallicity of $0.3\,Z_\odot$, being an order of magnitude higher than that predicted by Vink, de Koter

& Lamers (2001), after correcting the empirical mass-loss rate for wind inhomogeneities (Mokiem et al. 2007). Using the Vink et al. (2001) prescription for the WN star (MOD90) yields a much smaller discrepancy of a factor of ∼2. The discrepancy in the O-star mass-loss rate can be partly reconciled by taking a smaller number of brighter stars, for instance supergiants, in the following way. A brighter star has a larger radius. In order to preserve the Hα profile shape, the quantity $Q \propto \dot{M}/(R_*^{3/2} v_\infty)$ needs to remain invariant (de Koter, Heap & Hubeny 1998). This implies that for fixed temperature $\dot{M} \propto L_*^{3/4}$. However, the expected mass-loss rate scales as $\dot{M} \propto L_*^{2.2}$; therefore, a smaller number of brighter O stars may still match the strong Hα emission line wings and better reconcile observed and theoretical mass-loss rates. We did not pursue this strategy in view of the uncertainties that are involved, for instance those relating to the stellar mass (which enters the problem as mass-loss is expected to scale with mass as $\dot{M} \propto M^{-1.3}$). Moreover, we remark that higher than expected mass-loss rates have been reported for O stars in low-metallicity galaxies (Tramper et al. 2011).

7 SUMMARY AND CONCLUSIONS

We have analysed the VLT/X-shooter spectrum of C1_31, one of the most luminous sources in NGC 55, and its surroundings. We conclude that NGC 55 C1_31 is a cluster consisting of several massive stars, including at least one WN star, of which we observe the integrated spectrum.

The H, He I and He II lines in the stellar spectrum have been compared to synthesized spectra from a grid of FASTWIND non-LTE stellar atmosphere models. All normalized lines except He II λ 4686 can be reproduced by a single-star model with $T_{\rm eff} \lesssim 35\,000$ K, $\dot{M} \sim 2 \times 10^{-6}\,{\rm M}_\odot\,{\rm yr}^{-1}$ and $v_{\rm rot}\sin(i) = 150 \pm 50\,{\rm km\,s}^{-1}$. He II λ 4686 has an equivalent width of -3.6 ± 0.4 Å, but is ∼3000 km s^{-1} wide. No single-star model is able to produce matching profiles for all lines simultaneously.

An analysis of the nebular emission spectrum along the slit yields an electron density of $n_{\rm e} \leq 10^2\,{\rm cm}^{-3}$, electron temperature of T (O III) = 11 500 ± 600 K and oxygen abundance of [O/H] = 8.18 ± 0.03, which corresponds to a metallicity $Z = 0.31 \pm 0.04\,{\rm Z}_\odot$. A grid of CLOUDY models suggests that a hot (∼50 000 K) ionizing source is necessary to reproduce the observed T (O III) in an H II region with comparable density and metallicity.

We have also presented an illustrative cluster composition that reproduces all observed spectral features, the visual brightness of the target, and which is able to maintain an H II region with properties similar to those derived from the nebular spectrum. In our model, the cluster contains several blue (super)giants and one or more WN stars. While the proposed composition might not be unique, the presence of at least one very hot, helium-rich star with a high mass-loss is a robust conclusion. High angular resolution imaging reaching a resolution of 0.05 arcsec (corresponding to a physical distance of about 0.5 pc) would provide an improvement of a factor of 10–20 compared to our seeing-limited observations and would help to constrain the composition of the cluster. This makes NGC 55 C1_31 a prime target for 30-meter-class telescopes combining high angular resolution and integral field or multi-object spectroscopy.

ACKNOWLEDGMENTS

We acknowledge the X-shooter Science Verification team. We thank Andrea Modigliani and Paolo Goldoni for their support in data reduction. We also thank Christophe Martayan and Rudy Wijnands for helpful discussions as well as Norberto Castro and Grzegorz Pietrzyński for communicating updated photometry. We thank the referee for constructive comments.

REFERENCES

Asplund M., Grevesse N., Sauval A. J., Scott P., 2009, ARA&A, 47, 481
Baldwin J. A., Ferland G. J., Martin P. G., Corbin M. R., Cota S. A., Peterson B. M., Slettebak A., 1991, ApJ, 374, 580
Bestenlehner J. M. et al., 2011, A&A, 530, L14
Bresolin F., Pietrzyński G., Urbaneja M. A., Gieren W., Kudritzki R.-P., Venn K. A., 2006, ApJ, 648, 1007
Bresolin F., Urbaneja M. A., Gieren W., Pietrzyński G., Kudritzki R.-P., 2007, ApJ, 671, 2028
Cardelli J. A., Clayton G. C., Mathis J. S., 1989, ApJ, 345, 245
Castro N. et al., 2008, A&A, 485, 41
Crowther P. A., 2008, in Bresolin F., Crowther P. A., Puls J., eds, Proc. IAU Symp. 250, Properties of Wolf-Rayet Stars. Cambridge Univ. Press, Cambridge, p. 47
Crowther P. A., Schnurr O., Hirschi R., Yusof N., Parker R. J., Goodwin S. P., Kassim H. A., 2010, MNRAS, 1103
de Koter A., Heap S. R., Hubeny I., 1997, ApJ, 477, 792
de Koter A., Heap S. R., Hubeny I., 1998, ApJ, 509, 879
de Vaucouleurs G., Freeman K. C., 1972, Vistas Astron., 14, 163
D'Odorico S. et al., 2006, Proc. SPIE, 6269, 98
Evans C. J., Howarth I. D., Irwin M. J., Burnley A. W., Harries T. J., 2004, MNRAS, 353, 601
Evans C. J. et al., 2011, A&A, 530, A108
Ferland G. J., Korista K. T., Verner D. A., Ferguson J. W., Kingdon J. B., Verner E. M., 1998, PASP, 110, 761
Gieren W. et al., 2005, Messenger, 121, 23
Gieren W., Pietrzyński G., Soszyński I., Bresolin F., Kudritzki R., Storm J., Minniti D., 2008, ApJ, 672, 266
Goldoni P., 2011, Astron. Nachr., 332, 227
Gräfener G., Vink J. S., de Koter A., Langer N., 2011, A&A, 535, A56
Hummel E., Dettmar R., Wielebinski R., 1986, A&A, 166, 97
Kaaret P., Ward M. J., Zezas A., 2004, MNRAS, 351, L83
Kudritzki R. P., Hummer D. G., 1990, ARA&A, 28, 303
Kurucz R. L., 1979, ApJS, 40, 1
Kurucz R. L., 1993, VizieR Online Data Catalog, 6039, 0
Lamers H. J. G. L. M., Snow T. P., Lindholm D. M., 1995, ApJ, 455, 269
Lanz T., Hubeny I., 2003, ApJS, 146, 417
Martins F., Schaerer D., Hillier D. J., 2005, A&A, 436, 1049
Modigliani A. et al., 2010, Proc. SPIE, 7737, 56
Mokiem M. R., de Koter A., Puls J., Herrero A., Najarro F., Villamariz M. R., 2005, A&A, 441, 711
Mokiem M. R. et al., 2007, A&A, 473, 603
Moriya T., Tominaga N., Tanaka M., Maeda K., Nomoto K., 2010, ApJ, 717, L83
Osterbrock D. E., Ferland G. J., 2006, Astrophysics of Gaseous Nebulae and Active Galactic Nuclei. Univ. Science Books, Mill Valley, CA
Osterbrock D. E., Tran H. D., Veilleux S., 1992, ApJ, 389, 305
Pagel B. E. J., Simonson E. A., Terlevich R. J., Edmunds M. G., 1992, MNRAS, 255, 325
Pakull M. W., Angebault L. P., 1986, Nat, 322, 511
Pietrzyński G. et al., 2006, AJ, 132, 2556
Puls J., Urbaneja M. A., Venero R., Repolust T., Springmann U., Jokuthy A., Mokiem M. R., 2005, A&A, 435, 669
Rubin R. H., Simpson J. P., Haas M. R., Erickson E. F., 1991, ApJ, 374, 564
Sana H., Gosset E., Nazé Y., Rauw G., Linder N., 2008, MNRAS, 386, 447
Sana H., Momany Y., Gieles M., Carraro G., Beletsky Y., Ivanov V. D., de Silva G., James G., 2010, A&A, 515, A26
Savage B. D., Sembach K. R., 1996, ARA&A, 34, 279
Shirazi M., Brinchmann J., 2012, MNRAS, in press (doi:10.1111/j.1365-2966.2012.20439.x)
Stasińska G., 1990, A&AS, 83, 501
Stasińska G., Comte G., Vigroux L., 1986, A&A, 154, 352

Tramper F., Sana H., de Koter A., Kaper L., 2011, ApJ, 741, L8
Tüllmann R., Rosa M. R., Elwert T., Bomans D. J., Ferguson A. M. N., Dettmar R., 2003, A&A, 412, 69
Vernet J. et al., 2011, A&A, 536, A105
Vink J. S., de Koter A., Lamers H. J. G. L. M., 2001, A&A, 369, 574
Vink J. S., Muijres L. E., Anthonisse B., de Koter A., Gräfener G., Langer N., 2011, A&A, 531, A132
Walborn N. R., Fitzpatrick E. L., 1990, PASP, 102, 379
Webster B. L., Smith M. G., 1983, MNRAS, 204, 743
Zaritsky D., Kennicutt R. C., Jr, Huchra J. P., 1994, ApJ, 420, 87

This paper has been typeset from a TEX/LATEX file prepared by the author.